doi:10.26443/seismica.v5i1.2135

ISOLA-BaBoo, a code for full moment tensor inversion with uncertainty estimation; application to the 2025 Anydros earthquakes

Jiří Zahradník *[1], **Efthimios Sokos** [2], **Fatih Turhan** [3]

[1]Faculty of Mathematics and Physics, Charles University, Prague, Czech Republic, [2]Department of Geology, University of Patras, Patras, Greece, [3]Kandilli Observatory and Earthquake Research Institute (KOERI), Regional Earthquake-Tsunami Monitoring Center (RETMC), Boğaziçi University, Istanbul, Türkiye

Author contributions: *Conceptualization*: JZ. *Data Curation*: ES, FT. *Software*: JZ, ES. *Methodology*: JZ, ES. *Investigation*: JZ, ES, FT. *Writing – original draft*: JZ. *Writing – review and editing*: JZ, ES, FT.

Abstract Full moment tensors are important for revealing non-shear mechanisms of earthquake faulting. Nevertheless, non-double-couple components represent sensitive source parameters, less robust than strike, dip, rake, and moment. Thus, inversion of full moment tensors must be accompanied by uncertainty analyses. Here, we present a new version of traditional ISOLA software for inverting complete waveforms, in which uncertainty is analyzed with Bayesian bootstrap. This approach is particularly useful for obtaining uncertainty of model parameters without assuming a specific (e.g., Gaussian) distribution of data error and evaluating its covariance matrix. We assume that the set of recorded waveforms is representative, noise is low relative to the signal, and the velocity model is free of systematic error. The method is applied to 25 earthquakes of the 2025 Anydros crisis, Aegean Sea, Greece. Most of the analyzed events are Mw>4.5, and they consistently indicate a shear-tensile process, i.e., crack opening on mostly normal faults. The stress field calculated from these and previously published focal mechanisms is transtensional. The fault friction coefficient is low (~0.15). We preliminarily interpret the observed moment tensors as pointing to a fluid-assisted rupture process in a complex network of tectonic faults, likely triggered by a dike emplacement.

Production Editor: Andrea Llenos
Handling Editor: Matt Wei
Copy & Layout Editor: Théa Ragon

Received: November 10, 2025
Accepted: February 6, 2026
Published: February 18, 2026

1 Introduction

The 2024–2025 seismic crisis in the Santorini–Amorgos region underlined complex tectono-volcanic interactions. High-quality full moment tensors (MTs) of 133 events of Fountoulakis and Evangelidis (2025) have shown significant non-DC components, indicating fluid involvement. However, non-DC components represent sensitive parameters, less robustly inferred from seismic waveform measurements than standard source parameters, such as strike, dip, rake, and moment. Therefore, the focus of this paper is on a new uncertainty assessment of full MTs and application to the 2025 Anydros earthquakes. For this purpose, traditional ISOLA software (Zahradník and Sokos, 2018; Sokos and Zahradník, 2013; Zahradník and Sokos, 2025b) is upgraded here.

The non-DC components are isotropic ISO (= volumetric, VOL) and compensated-linear-vector-dipole CLVD. The absolute values of ISO and CLVD percentages, together with the always-positive DC percentage, sum to 100%. The six-parameter MT allows for mixed signs of ISO and CLVD in an event. The shear-tensile/compressional model, hereafter STC (Vavryčuk, 2011), allows only the same ISO and CLVD sign in an event. The STC model enables a phenomenological interpretation of MT in terms of shear faulting part (strike/dip/rake angles) and angular deviation of the slip vector from the fault plane, ranging from 0° to 90°/-90° for crack opening/closing, respectively. We invert waveforms of the Anydros sequence for six-parameter tensors and show that the estimated MTs can be interpreted in terms of the STC model. We also shortly discuss simpler deviatoric MTs that assume ISO=0, which may mask the true non-shear character of fault rupture. We use traditional MT characterization by DC, CLVD, and ISO percentages, yet more accurate representations exist, e.g. by means of the angular distance of an MT from pure DC, or from ISO on fundamental lune (Tape and Tape, 2012).

2 Method and data

2.1 MT inversion with covariance matrix

We calculate full moment tensors in a new software package, a conceptual update of ISOLA2024 (Zahradník and Sokos, 2025b). In ISOLA2024, the best-fit MT solution is calculated through a systematic space-time grid search of centroid position and time, with a least-squares inversion at every grid point. Centroid is a point-source representation of the earthquake estimated by waveform inversion. As shown below, the full MT calculation is straightforward if we know the cen-

*Corresponding author: Efthimios Sokos, esokos@upatras.gr

troid position and centroid time. Then the MT inverse problem is linear and can be solved analytically. The centroid and hypocenter usually differ from each other (due to source finiteness or measurement errors), implying a need to seek the centroid (position and time) in the vicinity of the hypocenter. Dependence of MT on position and time is non-linear, thus MT should be optimized over these parameters. Optimization over three space coordinates and time can be made deterministically with a grid search. The space grid is placed either vertically beneath the epicenter (as in applications of this paper) or in a more general way (e.g., in a 3D grid). Greens' functions, representing the medium response to impulsive forces, needed for all paths between space grid points and stations, are precalculated and stored in memory.

The MT inversion in a grid point is performed by the least-squares method (Tarantola, 2005). In ISOLA2024, we used equal station weights, yet explicitly involving a data-error covariance matrix $\mathbf{C_d}$:

$$\boldsymbol{m} = \left(\mathbf{G}^{\mathrm{T}}\mathbf{C}_{\mathrm{d}}^{-1}\mathbf{G}\right)^{-1}\mathbf{G}^{\mathrm{T}}\mathbf{C}_{\mathrm{d}}^{-1}\boldsymbol{d}. \quad (1)$$

In equation 1, $\boldsymbol{m}$ is the MT, $\mathbf{G}$ is the matrix of Green's functions, and $\boldsymbol{d}$ is the 3-component band-pass waveform displacement data at a set of stations. The data covariance matrix $\mathbf{C_d}$ is generally non-diagonal, thus potentially accounting for correlated data errors. Uncertainty of model parameters is investigated in ISOLA2024 analytically using the best fit solution $\boldsymbol{m}$ at each space grid point (optimized over time) and employing the theoretical covariance matrix of model parameters

$$\mathbf{C}_m = \left(\mathbf{G}^{\mathrm{T}}\mathbf{C}_{\mathrm{d}}^{-1}\mathbf{G}\right)^{-1}. \quad (2)$$

For details on how to employ $\mathbf{C_m}$ see equations 5-7 of Vackář et al. (2017). In that paper, the $\mathbf{C_d}$ matrix is estimated from pre-event noise, assumed to be Gaussian but not necessarily low. In ISOLA2024, a similar concept is adopted, but various other estimators of the data-error covariance matrix $\mathbf{C_d}$ are derived from residual waveforms, as inspired by Dettmer et al. (2007). Residual waveforms have also been used elsewhere to account for modeling errors, i.e., errors associated with imprecise velocity models (Poppeliers and Preston, 2022). ISOLA2024 is computationally demanding in both memory requirements and processing time. In general, the MT uncertainties derived from the estimated $\mathbf{C_d}$ matrix may appear unrealistically small—essentially overconfident—because the underlying estimates of data errors are themselves overly optimistic. For this reason, in the present paper, we adopt a conservative approach: we require that the noise level be low relative to the signal (or that the data be denoised before use), and we rewrite ISOLA around a fundamentally different concept that avoids strong assumptions about data errors.

2.2 MT inversion with BaBoo weighting matrix

In the new code, we employ the ordinary least-squares method to relate the weighted Green's functions, expressed as the matrix product $\mathbf{WG}$, to the equally weighted data $\mathbf{W}\boldsymbol{d}$, where $\mathbf{W}$ is a diagonal (generally non-constant) weighting matrix:

$$\boldsymbol{m} = \left((\mathbf{WG})^{\mathrm{T}}(\mathbf{WG})\right)^{-1}(\mathbf{WG})^{\mathrm{T}}\mathbf{W}\,\boldsymbol{d}. \quad (3)$$

Equation 3 is equivalent to 1 with $\mathbf{C_d}^{-1} = \mathbf{W^T W}$; i.e., $\mathbf{C_d}$ is a matrix formed by reciprocal values of squared weights; see Dodge (2008):

$$\boldsymbol{m} = \left(\mathbf{G}^{\mathrm{T}}\mathbf{W}^{\mathrm{T}}\mathbf{WG}\right)^{-1}\mathbf{G}^{\mathrm{T}}\mathbf{W}^{\mathrm{T}}\mathbf{W}\,\boldsymbol{d}. \quad (4)$$

Although the two methods, 1 and 4, appear to be formally identical, they are conceptually different. In 1, we assume that the data error is known, Gaussian, and represented by matrix $\mathbf{C_d}$, thus expressing a parametric likelihood model. Contrarily, in 4 we use an empirical, non-parametric error description, in which matrix $\mathbf{W}$ is formed by random samples of Bayesian bootstrap (BaBoo) weights. Many sets of weights are repeatedly applied, i.e., waveform data are repeatedly perturbed. For each data perturbation, equation 4 is solved across the space-time grid, producing an ensemble of solutions. In this way, random data variabilities (waveform perturbations), not the assumed data errors, are projected into model parameters. As Green's functions are precalculated, the repetition is fast; moreover, the individual perturbations can be calculated in parallel. The new code is called ISOLA-bootstrap, or ISOLA-BaBoo.

Seismological studies demonstrating the effectiveness of the Bayesian bootstrap for MT inversion remain relatively limited, with the GROND software representing a notable example (Heimann et al., 2018; Kühn et al., 2020). For a non-seismological application, see, e.g., Rodriguez and Williams (2022) and the blog https://www.sumsar.net/tags/bayesian/. GROND and other methods were used for benchmarking ISOLA-BaBoo, and one such test will be demonstrated below. The tests and applications are preparations for the implementation of ISOLA-BaBoo into automated, parallelized workflows.

2.3 Bayesian bootstrap

Here, we summarize the method using general statistical terminology. The observed waveform data are treated as independent realizations from an unknown distribution (F). Rather than assuming a parametric form for F, we adopt a Bayesian bootstrap approach (Rubin, 1981), in which random Bayesian weights are assigned to the observed sample. These weights define a nonparametric, Bayesian-weighted empirical approximation of the data-generating distribution. The resulting weighted sample is then used as input to the inverse problem.

We assume that the forward model is approximately correct, so that modeling errors are small and do not introduce a significant systematic bias. For each random draw of Bayesian-bootstrap weights, the inverse problem—both its least-squares component and its grid-search component—is solved by minimizing an L2-norm misfit between observed and predicted data. The L2 norm is used purely as a loss (misfit) function; it is not interpreted as arising from a Gaussian likelihood, nor do we assume Gaussian measurement errors.

The method yields a nonparametric, posterior-like distribution of model parameters obtained by propagating Bayesian-bootstrap uncertainty in the data through the inverse problem. This distribution reflects uncertainty in the empirical data distribution rather than a Bayesian posterior based on a prescribed parametric likelihood (Tarantola, 2005).

Bayesian bootstrap weights should not be interpreted as measurement errors. Instead, they quantify uncertainty about how well the available data represent the underlying distribution F. However, if measurement noise can be characterized and the data covariance matrix $\mathbf{C_d}$ can be reasonably estimated, the method can be extended by incorporating $\mathbf{C_d}$ — for example, by replacing $\mathbf{W^TW}$ with $\mathbf{W^TWC_d}^{-1}$ in the least-squares solution for model parameters. This may allow the approach to account for known correlated noise, while retaining its nonparametric Bayesian structure. Combining $\mathbf{W^TW}$ with $\mathbf{C_d}^{-1}$ and posterior exponential down-weighting is intended as a possible future upgrade and is not used in this paper.

For each bootstrap perturbation, the best-fit model (across the grid) is the optimal solution for that particular weighted data realization. To reduce overconfidence in a single best-fit model, we also consider, for each perturbation, a set of near-optimal grid points within a specified misfit threshold. This expanded ensemble captures additional model variability. To reduce the influence of models with substantially higher misfit, we can optionally apply a posterior exponential down-weighting of ensemble members as a function of their misfit. This step is not part of the Bayesian bootstrap itself; rather, it serves as a practical, partly subjective regularization that emphasizes better-fitting solutions while retaining the nonparametric character of the method.

2.4 Algorithm implementation

Technical details of the proposed method are as follows. The BaBoo technique is applicable to independent (uncorrelated) data. As the three recorded components at a station are dependent, we use station-level BaBoo weights, i.e., a weight is prescribed identically to all three components. An exception may be a component that must be removed from the inversion because of data problems, e.g., a clip; then the component weight is zero. Thus, the weighting matrix $\mathbf{W}$ is diagonal and remains constant across all time samples of all three components at each station. Accordingly, the weighting can be implemented explicitly in the code, eliminating the need to store or operate on the full sparse matrix $\mathbf{W}$. Therefore, the new code is formally as simple as the older ISOLA versions (Zahradník and Sokos, 2018).

The BaBoo weights (positive real numbers) are generated numerically as samples of Dirichlet distribution; the weights are normalized so that they sum to unity for each perturbation. They depend solely on the number of stations, not on the waveforms. Once a set of station weights is defined and applied to produce a data perturbation, we make a space-time grid search. It is assumed that the grid is sufficiently large and dense to likely include the true source position and time. At each point of the space-time grid, we solve equation 4, i.e., we invert the data to estimate the MT (with the BaBoo station weights). We quantify waveform fit with variance reduction, VR (always ≤1), symbolically written as $VR = 1 - \sum(\boldsymbol{o}-\boldsymbol{s})^2/\sum\boldsymbol{o}^2$, where $\boldsymbol{o}$ and $\boldsymbol{s}$ denote observed and synthetic waveforms, both equally BaBoo weighted, and summation is over all stations, components, and time samples. It represents a global L2-norm data fit.

The whole process is repeated NPER times (NPER is the number of perturbations, typically ~100). In this paper, we use NPER=100, sharing the same overall qualitative behavior of results as, for example, NPER=1000. From each perturbation, we accept a certain number of solutions of the highest VR values in that perturbation; hereafter, we denote this number NBEST. In other words, we sort the solutions in every perturbation according to VR, and take the NBEST top values. The solutions form a final ensemble, each ensemble member being characterized by the perturbation number, source position, source time, CLVD%, ISO%, six components of MT, and VR. From the ensemble of model parameters, we draw histograms, median values, and confidence intervals.

NBEST is a free parameter, controlling acceptance of near-optimum solutions, and is further extensively discussed in the real-data examples of the following sections. Before proceeding with the examples, we make a few notes about NBEST. The notes were inferred from synthetic tests using the `Forward Simulation` tool of ISOLA One of the space-time grid nodes was the assumed ("true") source. First, consider the inversion of synthetic noise-free data in an exact velocity model, i.e., with the same Green's functions used in the forward and inverse problem. In that case, NBEST = 1 returns the unique exact solution with VR=1 (the same for all perturbations). In the same setup, NBEST > 1 produces multiple solutions, including, besides the exact one, also non-exact MTs, with non-exact positions and times that also fit the data relatively well. Increasing NBEST, we still obtain one exact solution, and the number of solutions in non-exact positions and times may increase, particularly if a given earthquake has a trade-off between MT and centroid position. If we constrain inversion to the exact centroid position (and let centroid time vary), we obtain the exact solution plus other solutions with inexact time and inexact MT. Second, consider the inversion of synthetic noisy data or synthetic noise-free data inverted in an inexact velocity model. Then, NBEST = 1 cannot return an exact solution; it returns multiple non-exact (wrong) solutions of VR<1, varying during perturbations around the (wrong) solution with the largest VR. NBEST > 1 produces multiple non-exact solutions (varying positions, times, and MTs), and the true position and MT can be among them (with VR below the maximum VR), or not. These results imply that when dealing with real data, we should not overinterpret the best-fit solutions of the maximum VR = VRmax. That is the reason why we need the acceptance parameter NBEST > 1. Finally, let us comment on *a priori* constraining source position in synthetic tests. When constraining the position to the true value but

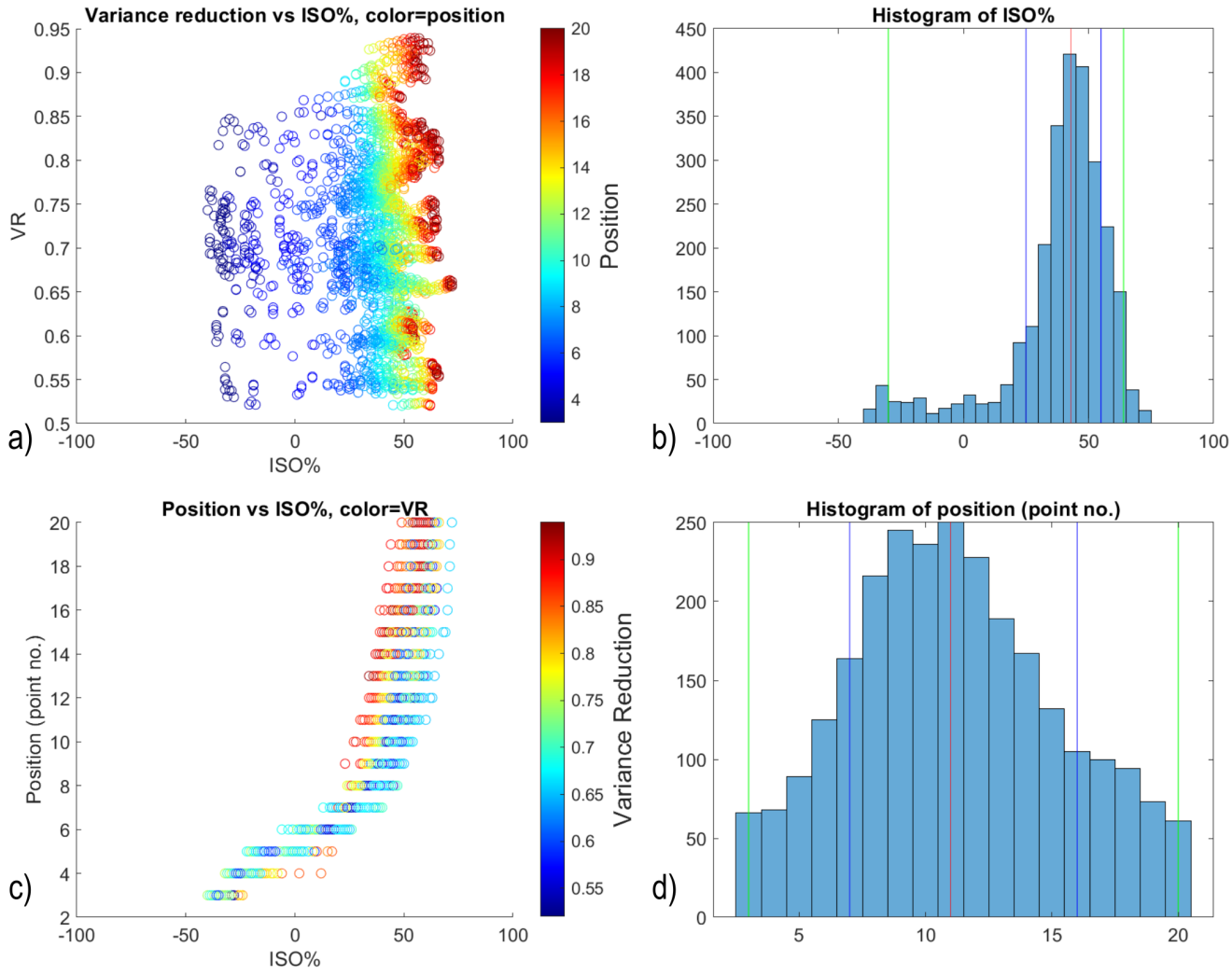

Figure 1 First example of ISOLA-BaBoo for the Mw 4.9 earthquake of 11/02/2025, origin time 11:43:54.22. Inversion performed with trial source positions 1-20 (depths below epicenter 1 – 20 km, step 1 km), and times -1.8 s to 1.8 s relative to origin time, step 0.3 s. Results of the probabilistic analysis with the formal parameter NBEST = 26 are demonstrated for ISO% and source position. VR is variance reduction: a) Variance reduction versus ISO and source position (color), b) Histogram of ISO, c) Position versus ISO and VR (color), d) Histogram of position. Vertical lines in histograms show the median (red) and the confidence intervals (68% blue and 95% green).

making inversion in an imprecise velocity model, we shall obtain incorrect MT and centroid time (both in the case of NBEST=1, or NBEST > 1). Later, in examples, we show that the major physical results, e.g., the median MT, may not significantly depend on NBEST, but the confidence intervals do depend on NBEST. A practically useful value of NBEST is about 10% of the tested space-time grid points.

2.5 Data processing

Here, we explain how the method is applied to data from Anydros sequence. ISOLA includes tools for manually selecting stations and preprocessing waveforms. Instead, in this paper, we use a semi-automated station selection from the Institute of Geodynamics, National Observatory of Athens (NOA), performed with the well-tested software GISOLA (Triantafyllis et al., 2015, 2021), http://orfeus.gein.noa.gr/gisola/realtime/2025/. We take this approach because Isola-BaBoo is intended for inclusion in a future upgrade of GISOLA; accordingly, the present paper functions as a pilot preparatory study. For the same reason, we rely on the pre-processed and instrumentally corrected full waveforms generated by GISOLA. A typical data set of a magnitude > 4 event consists of ~ 8-15 three-component broadband stations of the Hellenic Unified Seismological Network (HUSN; Evangelidis et al., 2021) at epicentral distances from ~40 km to ~300 km. We also use the manually revised epicenter location by NOA and set the trial source positions below that epicenter, and the trial source times around the origin time. Four 1D velocity models were tested in the present study, i.e., Novotný et al. (2001), Brüstle (2012), Dimitriadis et al. (2010), and a combination of the latter two provided by Fountoulakis (personal communication). Results for the latter velocity model are presented below. All tested models provide qualitatively similar results within the frequency range used (0.03-0.06 Hz). Long-term routine application for comparable magnitudes and distances has shown that this frequency range is reliable: noise is low

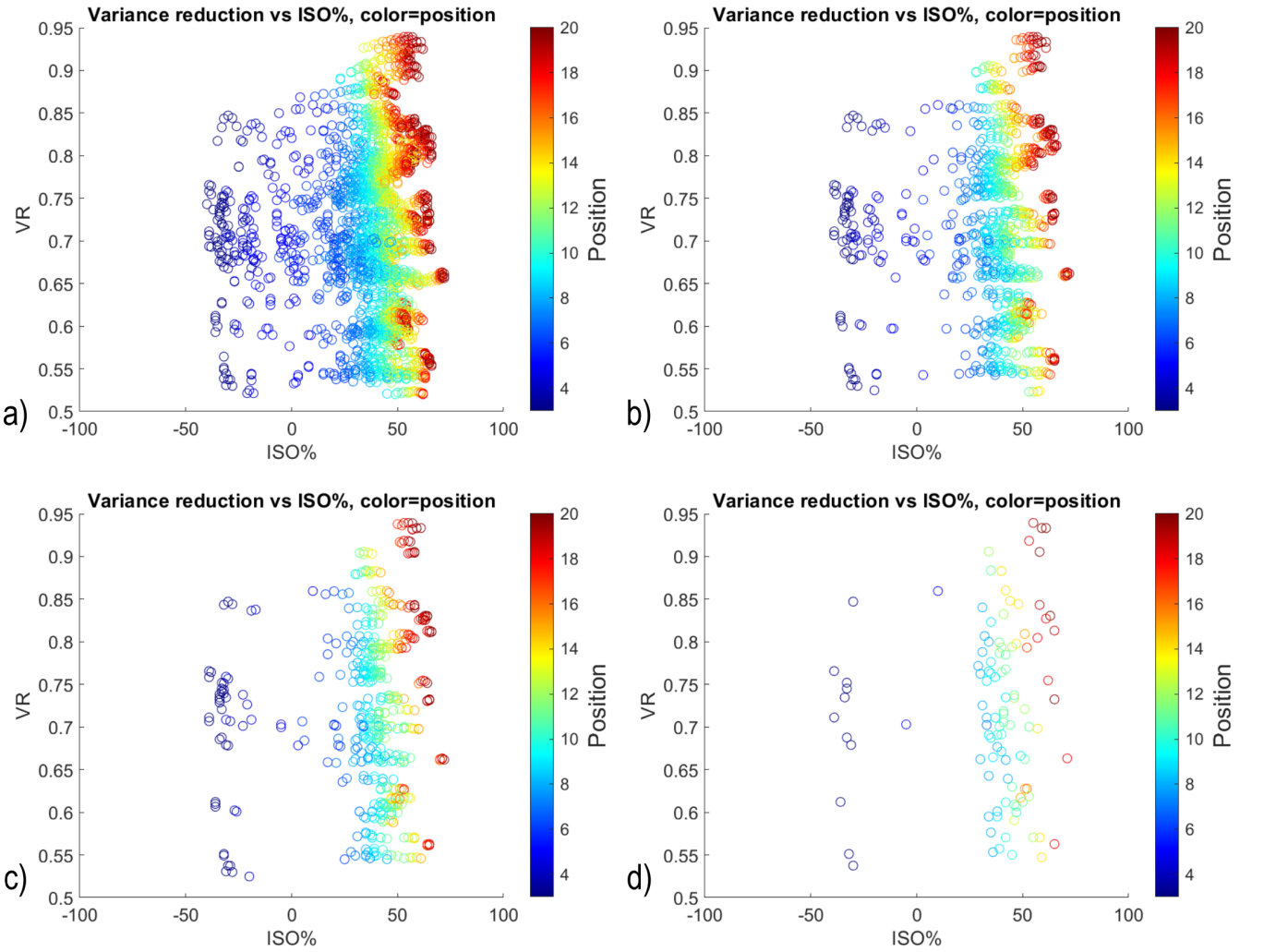

Figure 2 Continuation of the analysis of the Mw 4.9 earthquake of 11/02/2025, demonstrating variation of the results with the formal acceptance parameter NBEST: a) NBEST = 26 (10%) as in Fig. 1, b) NBEST = 10 (4%), c) NBEST = 5 (2%), d) NBEST = 1 (0.4%).

above 0.03 Hz, and velocity-model inaccuracies have only minor effects below 0.06 Hz. Indeed, inaccuracy effects scale with the ratio of epicentral distance to wavelength. With a maximum frequency of 0.06 Hz, all stations (closer than ~300 km) lie within six minimum S-wave wavelengths (3 (km/s) / 0.06 (Hz) ≈ 50 km). For larger distance-to-wavelength ratios, e.g., greater than about 15 or 20, the velocity-model inaccuracies typically prevent an acceptable waveform fit. Although inversion codes can, in principle, treat model error at larger distances and thereby capture MT uncertainty associated with imperfect Green's functions (e.g., Hallo and Gallovič, 2016), they still require velocity models whose departures from the true Earth structure do not exhibit systematic bias. Such techniques are not employed in this paper.

3 Two methodical examples

3.1 First example

In this section, we illustrate ISOLA-BaBoo on real-data examples of two events of the Anydros crisis. The first example is the Mw 4.9 earthquake of 11/02/2025, origin time 11:43:54.22 UTC, event No. 19 (we use event numbering introduced in Zahradník et al., 2025b,a). We invert full waveforms in 11 stations at epicentral distances from 40 to 250 km with good azimuthal coverage, in a frequency range of 0.03-0.06 Hz. In the following, we use the term "source position, or position number", because it is a general denotation of the space-grid nodes used in the code. We inspect 20 trial source positions (1-20, which in this case correspond to depths 1-20 km beneath the epicenter, step 1 km), together with 13 trial centroid times (between -1.8 s and 1.8 s relative to origin time, step 0.3 s); that is, 260 space-time grid points, in total. At each perturbation, we save NBEST=26 solutions (i.e., 10% of all grid points) of the highest VR in that perturbation; this acceptance rate is hereafter denoted as 26 (10%). All perturbations (NPER = 100) then create an ensemble of the NBEST × NPER accepted solutions. Solutions in the adopted ensemble have a highly variable data fit. This is a combined effect of the trial space-time variations and bootstrap; several perturbations contribute to the ensemble with the same space-time grid point, yet with different waveform fits (different VR), depending on the random station weights. Note that a space grid point is kept in the ensemble with dif-

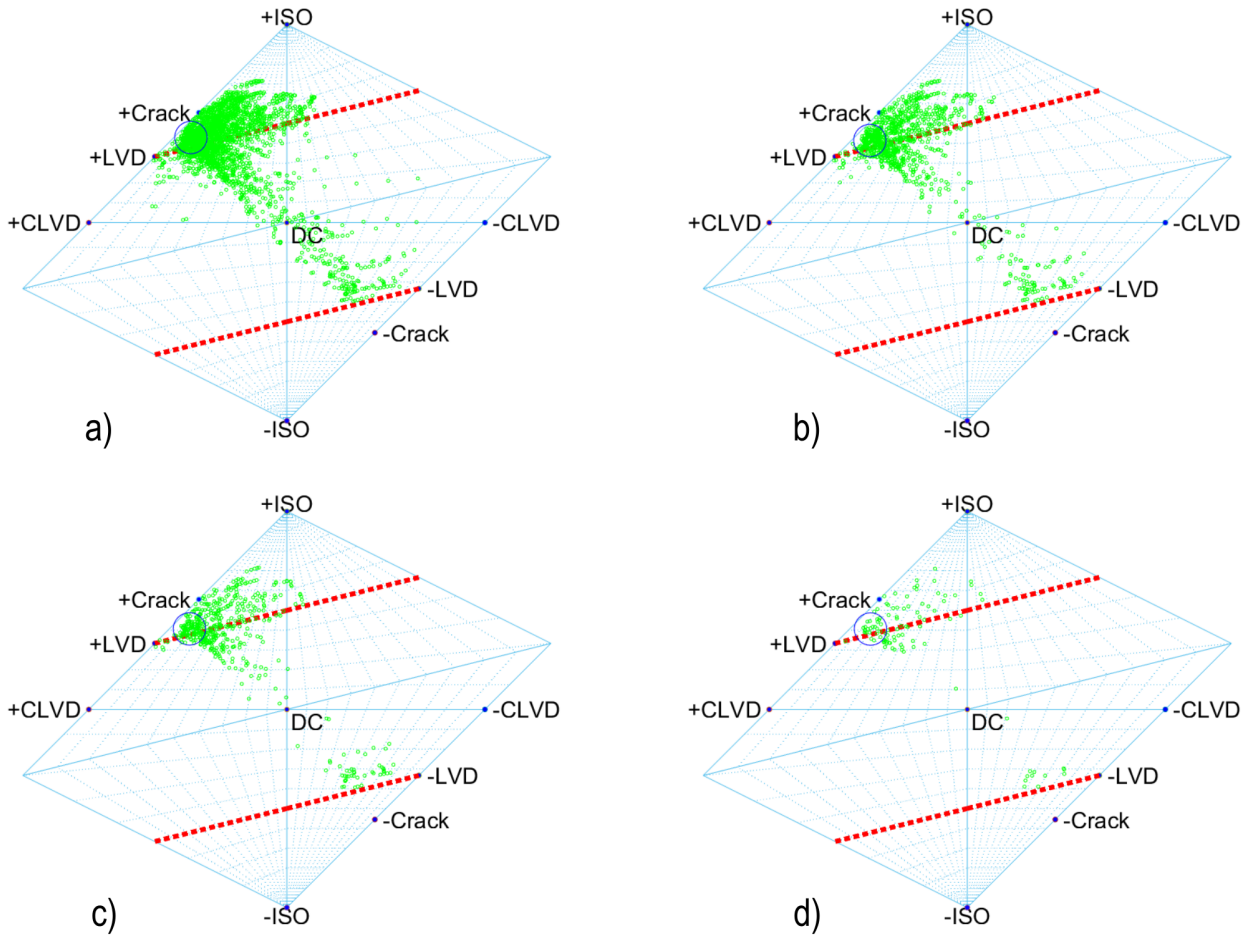

Figure 3 Continuation of the analysis of the Mw 4.9 earthquake of 11/02/2025, demonstrating variation of Hudson's source-type plots with the formal acceptance parameter NBEST: a) NBEST = 26 (10%) as in Fig. 1, b) NBEST = 10 (4%), c) NBEST = 5 (2%), d) NBEST = 1 (0.4%). Each green point is an MT solution, a member of the ensemble resulting from the BaBoo MT inversion. While the scatter and range of the solution ensemble depend on the misfit acceptance threshold, controlled by NBEST, we find that the median moment tensor (shown by a blue circle) is nearly invariant to NBEST. It indicates a robustly resolved non-DC source type with significant ISO > 0 and CLVD > 0. Nevertheless, due to the broad range of trial source positions 1-20, the solution is ambiguous, featuring also secondary solutions with ISO < 0 and CLVD < 0. For reduced ambiguity, see Fig. 4.

ferent times, without optimizing the fit over time at that point, and vice versa. Therefore, the VR range across all perturbations is broad (see Fig. 1a with VRmin = 0.5 and VRmax = 0.95). Also note that the VRmin and VRmax values are not known before inversion.

Although the total number of grid points (260) is not large, the ensemble created in 100 perturbations (2600 values) is more than sufficient to recognize the distribution of model parameters. For example, as seen in both Fig. 1a and 1b, the ensemble indicates that most solutions have ISO ~ 50% (i.e., 40% - 60%), independently of VR. The most frequent source position number is 11, or 7-16 (see Fig. 1a – symbols near the center of the color bar, and histogram of accepted solutions in Fig. 1d); as noted above, here it means 11 km, or 7-16 km. The ensemble also contains less abundant MTs with positions ~20 and ~4 (the darkest red and blue symbols in Fig. 1a, respectively). These are of two different types, which can be identified in Fig. 1a and 1c: Positions ~20 (or > 14), correspond to a narrow interval of ISO values just slightly greater than the dominant ISO ~50%. A narrow range of very well-fitting solutions near VRmax, e.g., 0.9 to 0.95, does contain these positions (see the top part of Fig. 1a). Contrarily, positions 4 (or < 7), correspond to highly spread values of ISO%, including ISO ≤ 0, quite different from the dominant ISO ~ 50%, and these solutions (VR < 0.95) do not belong to the range very near to VRmax.

While this example used the option NBEST = 26 (10%), analogous results can be obtained with NBEST = 10 (4%) or 5 (2%), (Fig. 2a-c). The prevailing positions 7-16 and their ISO ~50%, as well as the VR range, are nearly the same as those for the NBEST = 26 choice. With NBEST=26, the dense ensemble clearly reveals that besides the dominant ISO ~50%, we also obtain a secondary group of solutions in a relatively broad range of ISO from -30% to 30% (Fig.1b), causing ambiguity in source type. Contrarily, if choosing just a single best-fit solution of each perturbation, NBEST=1, the ensemble is basically the same, just too sparse with the used uniform grid (Fig. 2d). The same is true for other MT parameters, e.g., CLVD values, centroid times, etc. Conse-

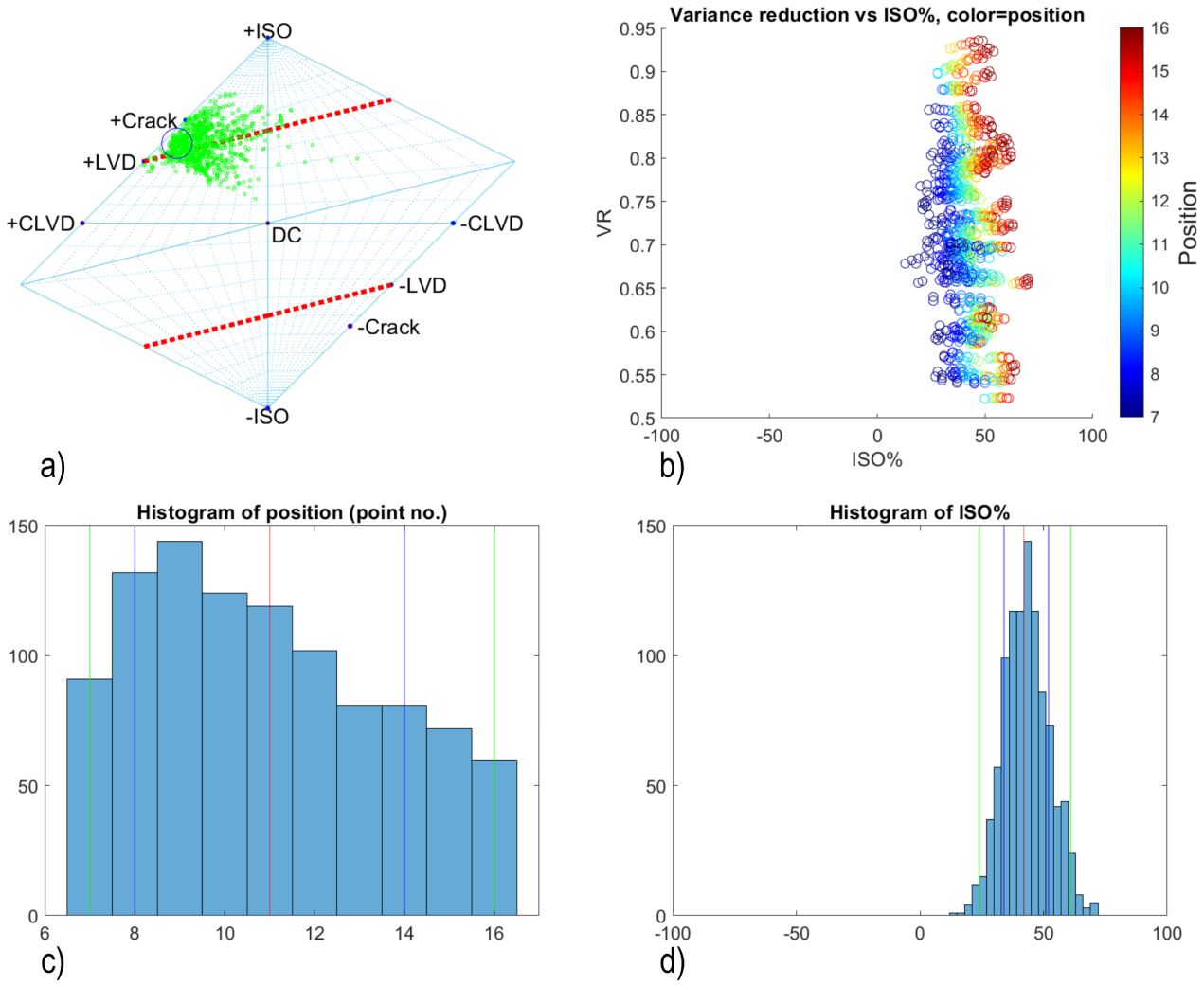

Figure 4 Continuation of the analysis of the Mw 4.9 earthquake of 11/02/2025. An additional inversion in the reduced range of positions 7-16, suggested by the 68% confidence interval of Fig. 1d, and using NBEST = 10 (8%). a) Source-type plot, b) Variance reduction versus ISO and position (color), c) Histogram of position, d) Histogram of ISO. Symbols as in Fig. 1.

quently, source-type plots (Fig. 3) vary with NBEST, but median MT remains stable.

The observed trade-off between MT and position (e.g., Fig. 1c) suggests ways to suppress or reduce ambiguity of the source type. One way is to rely on accurate earthquake location, which can be used to constrain the range of tested source positions. The other way is to start with initial MT inversion in a broad position range, as in the above example, recognize the depth-dependent ambiguity of source types, and perform an additional inversion in a reduced interval of trial positions. The reduced interval of positions can be, for example, that with VR near VRmax (positions 14-20 in our example); however, it may be risky because the MTs with the relatively rare VRmax might be biased due to data errors and inaccuracies of velocity models. More robust MTs can be obtained if making additional inversions in the reduced interval of trial source positions that dominated the initial inversion and provided a stable ISO and CLVD, invariant with VR, detailed as follows.

Continuing in our first event example, we demonstrate the additional inversion constrained to positions 7-16; these values were obtained as limits of the 68% confidence interval in Fig. 1d. We arbitrarily chose NBEST = 10 (8% from the current 130 space-time grid points), and the result is shown in Fig. 4. Note that a greater NBEST would make histograms even smoother, not changing the physical results. Compared to Fig. 1b, restricting the search to positions 7–16 suppresses the solution ambiguity associated with the ISO sign; now we have only ISO>0. The median moment tensor remains essentially unchanged, but the confidence intervals become narrower while still retaining solutions with VR values close to VRmax. The source considerably deviates from pure shear (DC). The source-type plot (Fig. 4a) features most of the solutions (green dots) with ISO > 0 and CLVD > 0. The same signs indicate the applicability of the STC model.

Validation of the method is presented in Fig. 5. It can be used for comparing our BaBoo solution of Fig. 4a to those from four independent approaches: GROND of Heimann et al. (2018), Fig. 5a, and ISOLA2024 with covariance matrices $\mathbf{C_d}$ of types 1, 2, 3 of Zahradník and Sokos (2025b), Fig. 5b-d. They all confirm the same non-DC MT type with ISO > 0, CLVD > 0, although the best-fit depth varies across the methods from 7 to 14 km. Our BaBoo solution would be close to that of GROND at

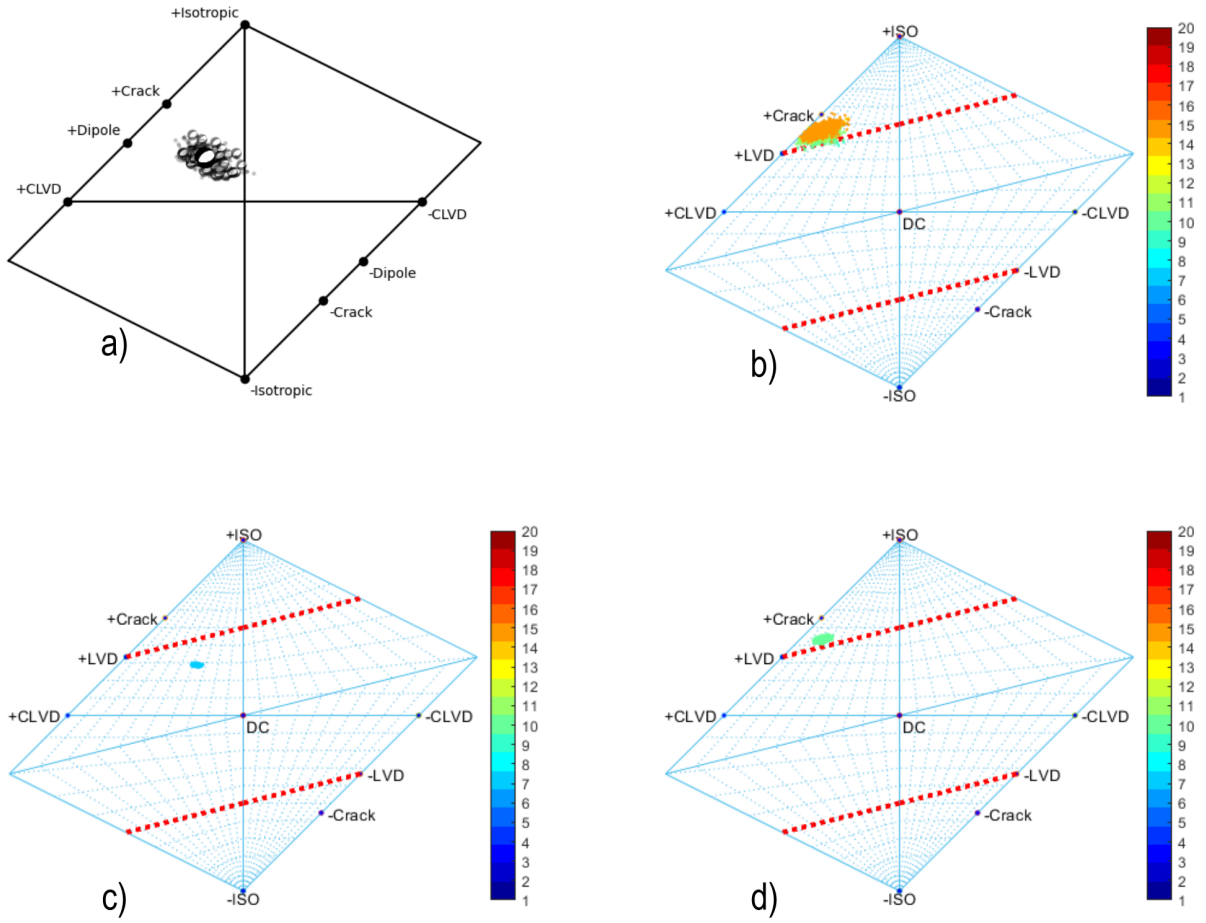

Figure 5 Continuation of the analysis of the Mw 4.9 earthquake of 11/02/2025. Validation of Fig. 4a by comparison of source-type plots from four alternative methods. a) GROND (optimal calculated depth of 7.8 km), and three methods of ISOLA2024, color-coded with source positions and based on different types of the data covariance matrix $\mathbf{C_d}$: b) $\mathbf{C_d}$ of type 1, i.e., a constant-diagonal covariance matrix, sometimes also called "no covariance matrix", "no-cova", c) $\mathbf{C_d}$ of type 2, the residual variance matrix with exponential off-diagonal decay, d) $\mathbf{C_d}$ of type 3, the Toeplitz matrix from the autocovariance function of the residuals; for details of b-d, see Zahradník and Sokos (2025a). Kagan angle deviation of the DC part of the best MT in Fig. 5a and median MT in Fig. 4a is 13°.

depths near 7 km. The solutions of Fig. 5, particularly Fig. 5c and 5d, are more "focused" in a narrow cloud in Hudson's plot than our solution in Fig. 4a. It is because of their implicit preference for the highest VR values, and the adopted estimates of the data error matrix $\mathbf{C_d}$. In Fig. 4a, with BaBoo approach, the uncertainty estimate is more conservative; we obtain a broader range of acceptable depth and MTs, because we do not impose any assumption on the data-error distribution. BaBoo calculations for Fig. 4 are considerably faster and less memory demanding than those of Fig. 5b-d.

Finally, to provide a first glance at stability, we compare the resulting one-sigma confidence intervals of ISO% (34, 52) and CLVD% (23, 47) in this example (Fig. 4) with a test in which, instead of BaBoo, we weighted all stations equally and did not analyze uncertainty. In such a test with full MT we obtained ISO=44% and CLVD=48%.

3.2 Second example

The second example is the Mw 5.2 earthquake of 12/02/2025, origin time 01:14:54.63 UTC, event No. 20. Trial positions 1-20 (depth 1-20 km) and times -1.8 to 1.8 s relative to origin time, step 0.3 s, are chosen as in the first example. The initial inversion (not shown) indicated a narrow 68% confidence interval of positions 3-6. Fig. 6 is the inversion in a reduced interval of positions 3-6, using NBEST= 10 (19% of the 52 trial grid points). In Fig. 6a, the solutions cluster on the opposite side of Hudson's plot relative to Fig. 4a, clearly indicating the opposite non-DC character of the source process, with ISO < 0, CLVD < 0.

4 Application to Anydros

4.1 Previous studies

Seismic source studies and tomography investigations contribute to understanding the interplay between tec-

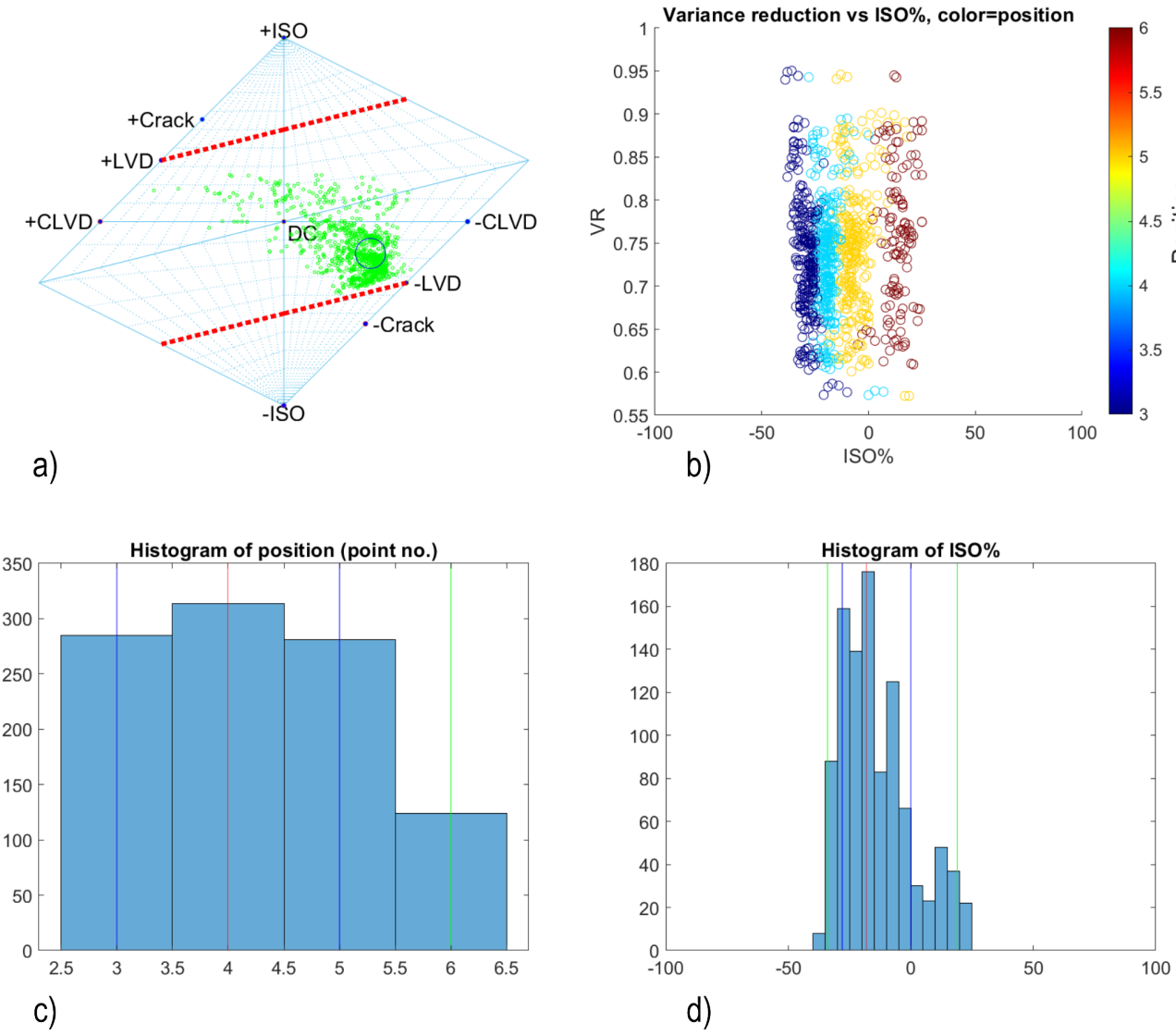

Figure 6 Second example of ISOLA-BaBoo for the Mw 5.2 earthquake of 12/02/2025, origin time 01:14:54.63. Graphic arrangement as in Fig. 4. An initial inversion for positions 1-20 (not shown) suggested dominance of the solutions in the range of positions 3-6. Here, the inversion is performed with such a reduced range (i.e., trial sources below epicenter at depths 3 – 6 km, step 1 km), and times -1.8 s to 1.8 s relative to origin time, step 0.3 s. Results of the probabilistic analysis with NBEST = 10 (19%).

tonic and volcanic processes (e.g., Schmid et al., 2022; Autumn et al., 2025). Precise relocations of small earthquakes between 2002 and 2019 in the Santorini-Amorgos zone by Andinisari et al. (2021a) delineated several fault zones but also revealed vertical clusters of hypocenters beneath the island of Anydros. Moment tensors of microearthquakes below Anydros revealed positive non-double-couple (non-DC) components associated with the opening of cracks and negative components (crack closing) beneath Kolumbo volcano (Andinisari et al., 2021b). Elevated Vp/Vs ratios 1.77–1.86, calculated from seismic travel times by Andinisari et al. (2021a), were interpreted in terms of crack density and fluid saturation. Thus, Andinisari et al. (2021a) suggested that regional extensional deformation hosts pathways for upward-migrating fluids, representing an indication of emerging volcanic activity. Similar conclusions were made for the Kolumbo volcano (Schmid et al., 2022). Shallow P-wave tomography of Heath et al. (2019), at depth < 3 km, has shown reduced seismic velocities near Anydros, possibly due to extensive SW-NE faulting; regional magmatism has been localized in NE-SW trending basin-like structures, pointing to an interaction between magmatism and active deformation. Fluid and magma involvement in the 2024–2025 seismic crisis in the Santorini–Amorgos region was signaled by non-DC full moment tensors of Fountoulakis and Evangelidis (2025) and Zahradnik et al. (2025); Zahradník et al. (2025a,b).

4.2 Non-DC components and uncertainty

Here we present results for 25 earthquakes that occurred near Anydros Island in 2025. The events were pre-processed by GISOLA, and represent most of the (34) NOA magnitude ≥ 4.5 events located in the Anydros region between February 2 and 18, 2025; see Fig. 7a. Using the NLL-SSST-coherence location results of Lomax (2025), followed by HypoDD relocation

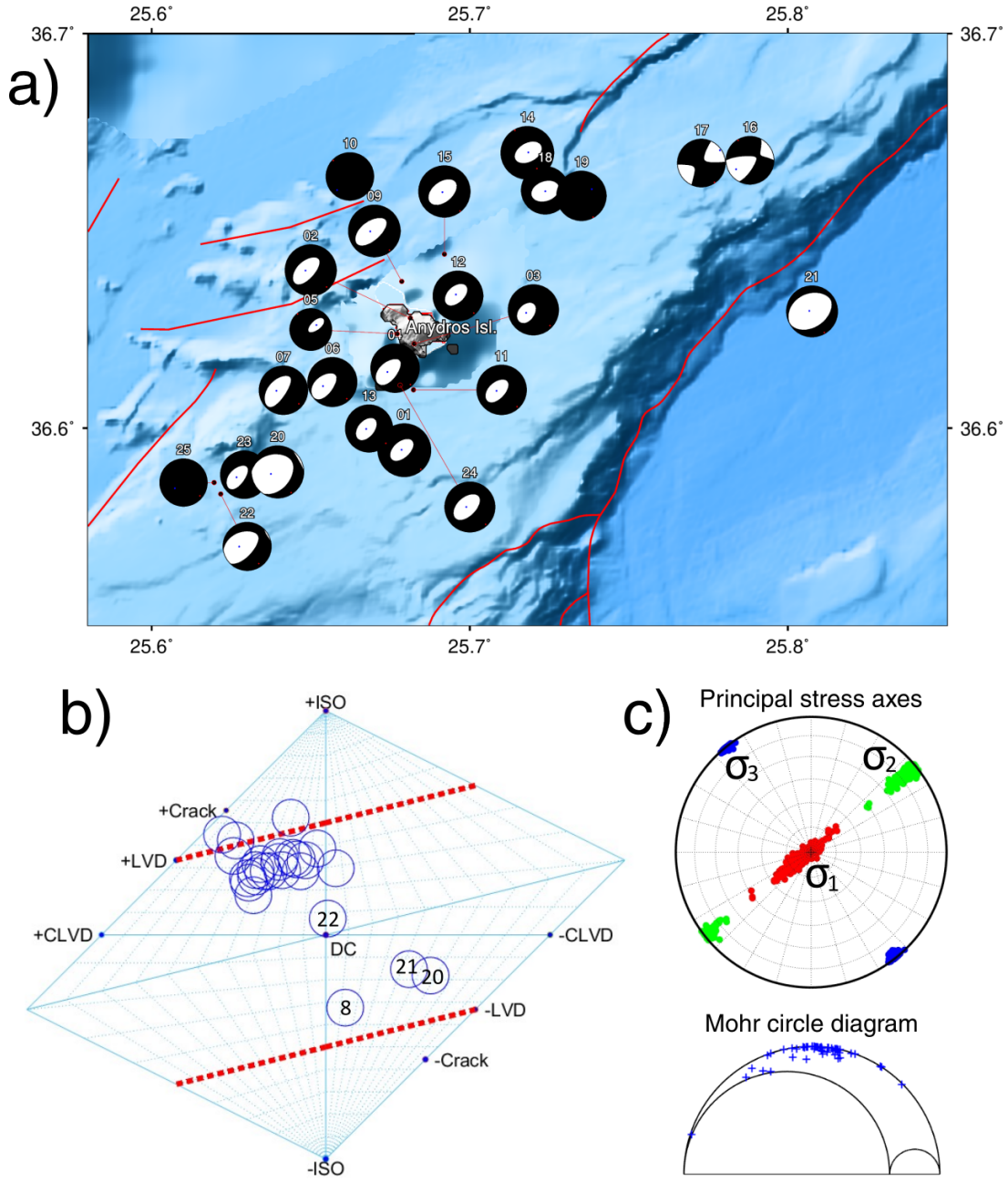

Figure 7 Analysis of 25 Anydros earthquakes. a) Full moment tensors ("beachballs"); faults (red lines) are from the NOAFAULTS v5.0 database (Ganas, 2023). b) Source-type plot of the analyzed earthquakes, each one represented by its median moment tensor (blue circle). For MT uncertainties and event numbering, see Table 1; the numbers are plotted only outside the main cluster of the open-crack events. Nos. 20 and 21 are closed-crack events, No. 22 is a near-DC event, and No 8 is a poorly resolved event. c) Principal stress axes (σ_1 red, σ_2 green, and σ_3 blue), and Mohr's diagram.

(Waldhauser, 2001; Waldhauser and Ellsworth, 2000) the depths were constrained (Z. Roumelioti, personal comm.): we searched depths 7-20 km for events 1-19, and 1-20 km for events 20-25, using depth step of 1 km. Each blue circle in Fig. 7b is a median MT of an event. For numerical values and confidence intervals, see Table 1. As demonstrated in Fig. 7b, the waveform inversion unambiguously provides the full MTs with ISO > 0 and CLVD > 0 for most of the investigated events. Note also that blue circles are tightly clustered in Fig. 7b. This indicates robustly resolved non-shear faulting, stable across the events. The positive signs of ISO and CLVD point to the shear-tensile source process, i.e., crack opening. Analogical dominant mechanism was also found by Isken et al. (2025). Two events (numbered 20 and 21 in Fig. 7b) represent a shear-compressional process, i.e., crack closing (ISO < 0, CLVD < 0). Such mechanisms were not discussed by Isken et al. (2025). We did not observe enough events of this type to discuss them in greater detail, e.g., whether they preferentially occur at shallower depths or not. One event was poorly resolved (No. 8). The two examples of the previous methodical sections correspond to events No. 19 (inside the main non-numbered cluster of Fig. 7b) and No. 20.

Non-DC components of an MT can be used for estimating the volume change involved in a fault rupture (Dahm and Krüger, 2013). For a single typical magnitude 5 event of our set, with positive non-DC, we ob-

Date	Mw	ISO (%)			CLVD (%)			Depth (km)			Strike Dip Rake (°)		
No01 2025/02/04 13:04:14.56	5.25	24	**36**	46	-1	**16**	27	9	**11**	13	235	39	-81
No02 2025/02/05 19:09:38.62	5.05	18	**29**	42	9	**29**	39	7	**9**	10	241	35	-69
No03 2025/02/03 09:29:42.49	4.95	19	**39**	58	-41	**3?**	19	7	**9**	14	250	40	-52
No04 2025/02/03 20:19:39.39	4.77	15	**29**	42	3	**21**	42	7	**9**	11	255	43	-49
No05 2025/02/08 16:30:00.76	4.02	19	**35**	51	-6	**17**	35	7	**9**	14	205	52	-126
No06 2025/02/08 09:00:41.37	4.83	15	**27**	42	13	**26**	37	7	**8**	11	263	44	-40
No07 2025/02/07 07:16:13.66	4.77	12	**25**	44	16	**36**	50	7	**9**	13	243	31	-59
No08 2025/02/02 23:54:41.58	4.18	-43	**-26**	-1	-38	**6**	56	7	**9**	17	253	69	-79
No09 2025/02/09 19:05:39.41	5.13	16	**26**	34	22	**29**	37	7	**8**	10	244	40	-73
No10 2025/02/05 17:47:28.04	4.67	43	**51**	60	-4	**8**	28	7	**8**	10	266	76	-19
No11 2025/02/04 02:46:06.98	4.86	18	**33**	45	-1	**17**	32	8	**10**	12	244	38	-67
No12 2025/02/03 12:17:40.53	4.92	18	**34**	46	-5	**14**	27	9	**11**	13	230	37	-87
No13 2025/02/02 17:45:44.99	4.62	19	**35**	49	-12	**8**	24	7	**9**	10	230	39	-78
No14 2025/02/10 20:16:29.37	5.24	16	**33**	45	-10	**7**	21	7	**9**	11	238	45	-94
No15 2025/02/10 22:37:25.55	5.08	13	**28**	43	-13	**6**	20	8	**9**	11	238	43	-81
No16 2025/02/10 11:23:17.71	4.68	8	**17**	26	19	**32**	42	10	**12**	14	279	71	-25
No17 2025/02/11 05:58:44.81	4.68	17	**23**	32	18	**32**	45	10	**11**	13	191	84	-177
No18 2025/02/11 07:17:19.00	4.67	8	**29**	45	-19	**1?**	15	8	**10**	12	251	48	-88
No19 2025/02/11 11:43:54.22	4.88	34	**43**	54	22	**37**	48	8	**10**	16	206	55	-144
No20 2025/02/12 01:14:54.63	5.18	-28	**-19**	8	-53	**-45**	-9	3	**4**	5	259	43	-58
No21 2025/02/18 04:46:52.13	5.05	-31	**-15**	26	-49	**-35**	-11	4	**5**	7	247	40	-80
No22 2025/02/12 08:29:48.29	4.72	14	**7**	26	-28	**3?**	21	3	**6**	8	265	35	-49
No23 2025/02/12 09:15:07.42	4.65	8	**31**	39	4	**26**	36	5	**8**	14	254	38	-48
No24 2025/02/17 07:49:51.04	4.94	5	**29**	45	-16	**15**	43	6	**8**	11	237	38	-77
No25 2025/02/18 06:08:08.96	4.64	24	**38**	50	12	**28**	42	4	**5**	7	254	44	-37

Table 1 ISO, CLVD, and depth are given with their median (in bold), and confidence interval (± 1-sigma). Mw, and strike/dip/rake angles refer to the median MT. "No" is an internal numbering of events in this study. CLVD with a question mark symbol is a value modified by a few percent to have the same sign as ISO, as required in the STC model. Events 1-19 were inverted in depths 7-20 km (step 1 km), events 20-25 in depths 1-20 km (step 1 km). No. 8 (shaded) is a poorly resolved event. No. 20 and 21 are the two shear-compressional events; all the others are shear-tensional.

tain an opening of about 10^5 m^3, i.e., of about 10^6 m^3 for the whole crisis. An effective order-of-magnitude model corresponding to the 10^5 m^3 crack opening could be, for example, a 1000 m x 1000 m x 0.1 m co-seismically opened fault space (possibly filled with a fluid). Typical positive ISO and CLVD values of our set, interpreted in terms of the STC model, indicate a fault opening angle (the angle between slip vector and fault plane) of about 10°-20°.

The DC part of the focal mechanisms of all analyzed events is mostly normal faulting, but a few strike-slip events were also found (Table 1 and Fig. 7a). Combining our focal mechanisms with ~30 focal mechanisms computed by NOA and retrieved via EMSC for the 2025 Anydros crisis, we obtained (code StressInverse of Vavryčuk, 2014) a transtensional regional stress field, shown in the upper part of Fig. 7c. Typical SW-NE trending fault structures of the region are nearly perpendicular to the minimum principal stress axis. The stress shape ratio is 0.2. A remarkable result is a very low friction coefficient of ~ 0.15, indicated by the presence of most events at the top of Mohr's circle; see the lower part of Fig. 7c.

The seismically released moment of the whole crisis is ~$1.5.10^{18}$ Nm, equivalent to a single Mw 6.1. However, the geodetic estimate is much greater, of about ~$2{\cdot}10^{19}$ Nm, equivalent to Mw 6.8 (Bufféral et al., 2025; Briole et al., 2025).

5 Discussion

5.1 Possible interpretations

At this stage, we cannot fully explain the non-shear faulting of the Anydros crisis, so here we provide a discussion of possible interpretations as a guide for future research. While the non-zero isotropic components have been observed globally, their sign and relation to the tectonic-volcanic process remain ambiguous. Generally, an ISO > 0, as an indicator of a fluid-filled crack opening, can be produced on faults, dikes, or both. For example, the fluid-filled crack may be a magmatic dike near a fault; shear rupture of the fault produces a fast dike volumetric increase (Dahm and Brandsdóttir, 1997). The observation of ISO > 0 for strike-slip events in Iceland (Büyükakpınar et al., 2024) has been interpreted as "an interaction between magmatic intrusions and the derived magmatic gases with shear fractures in the dike damage zone". Cyclic surface motions and seismic activity in Iceland have been explained as due to the migration of deep magmatic fluids and gases (of mantle origin) into upper crustal hydrothermal systems

(Flóvenz et al., 2022). Some observations in Iceland at depths of 2-5 km reported ISO < 0 for normal events and ISO > 0 for reverse ones (Hrubcová et al., 2021). Normal faulting correlating with ISO > 0 has been found near injection wells in The Geysers geothermal reservoir, interpreted as tensile opening due to lower differential stresses than in reverse faulting (Martínez-Garzón et al., 2017).

The standard idea is that faults can be triggered by a decrease in effective normal stress due to pore-pressure increase (e.g., Vavryčuk, 2015). A non-standard modern hypothesis based on an in situ small-scale cross-borehole fluid-injection experiment and numerical models states that a key factor in fault opening is a slip-induced increase of permeability (after initial fault failure); the latter yields a final massive fault opening, see Cappa et al. (2022). Whether this mechanism was behind the relatively large positive ISO and CLVD values observed in our study remains to be validated by a quantitative assessment of the hydraulic parameters and numerical modeling of the fault opening.

A closely related question is how to explain the observed low friction coefficient. Faulting under near-zero friction (Tresca's failure criterion) has been observed in the laboratory (Rutter et al., 2013). Another laboratory experiment (Dou et al., 2020) revealed a decrease in friction due to fault lubrication, feasible even under low pore pressure. Although these mechanisms remain debated for real faults, the latter may be applicable in our region because fluid presence in the faults is independently shown by the fault opening.

Stress transfer between faults and dikes is a phenomenon directly affecting the space-time seismicity distribution. Complex space-time migration episodes were reported for the Anydros crisis (e.g., Fountoulakis and Evangelidis, 2025; Hufstetler et al., 2025; Karstens et al., 2025), with speeds occasionally exceeding 1 km/h. Such a migration, faster than pore-pressure diffusion, might be explained by slow aseismic fault motions (Dublanchet and De Barros, 2021). The importance of aseismic stress transfer seems to be indicated for Anydros also by the above-mentioned geodetic estimate of total released moment, exceeding by an order of magnitude the seismic moment (Bufféral et al., 2025). Indeed, Ganas et al. (2025) and Briole et al. (2025) have modeled the geodetically measured displacements and proposed a significant slow-slip motion along a SE-dipping normal fault between Santorini and Anydros. We speculate, but again need future numerical modeling, that such a slow slip might have triggered the part of the 2025 crisis beneath Anydros Island, which comprised most Mw>4.5.

Alternatively, Karstens et al. (2025), and later also Isken et al. (2025), interpret most activity beneath Anydros as due to a ~13 km long dislocation, representing an emplaced dike which opened a volume of ~0.3 km^3. Analogously, Karakostas et al. (2025) and Lomax et al. (2025) proposed a thin vertical tensile source (a horizontally propagating dike) and its Coulomb stress effect as a possible trigger of the massive seismicity beneath Anydros. Anyway, a physics-based model explaining the non-DC MT components near Anydros is still lacking, and the mechanisms by which individual normal-fault ruptures might incorporate an opening component remain unresolved.

5.2 A warning about deviatoric MT inversion

MT inversions under deviatoric constraint (assuming ISO=0) are applied in routine MT calculations by many agencies, e.g., NOA or GCMT (Global Centroid Moment Tensor project; Dziewonski et al., 1981; Ekström et al., 2012). For the Mw 5.3 event No. 1 of this paper, 2025/02/04 13:04:14.56, GCMT reported CLVD = 1%, i.e., DC= 99 %, an almost pure shear faulting, strongly contrasting with the full MT of this paper (median ISO of 36% with the 68% confidence interval from 24% to 46%, median CLVD of 16%, from -1% to 27%). When we calculate deviatoric MT for event No. 1, similarly to GCMT, we also obtain a large DC% = 80 at nearly the same variance reduction as that of full MT. In other words, if an earthquake contains a significant ISO component and is inverted as deviatoric, it may result in an erroneous CLVD% and DC%. Thus, under the deviatoric assumption, the detection of non-shear-faulting may completely fail. This issue has been explained through synthetic tests accompanying the previous calculations of non-DC in the Santorini region (Křížová et al., 2013, 2016). That is one of the reasons why we focused this paper on the methodology of full MT inversions and their uncertainties. Whether seismic agencies should solely report full MTs is a complex question. As this example illustrates, deviatoric inversion can yield erroneous results. At the same time, full MT inversion is often numerically less well posed than its deviatoric counterpart, and it does not necessarily yield a better fit to the data. A practical strategy is to compute both solutions and, when they diverge, treat the event as requiring special scrutiny beyond the routine workflow.

6 Conclusion

We have developed and tested a new ISOLA version for full MTs with uncertainty assessment based on Bayesian bootstrap; ISOLA-BaBoo. Conceptual simplicity (no need to estimate and store data covariance matrices) and computational speed make it potentially useful for automation and routine use in seismic agencies.

The application to real data resulted in the following qualitative interpretation: Beneath Anydros, the zone with the massive occurrence of larger events (Mw>4.5) appears to be a complex network of mainly normal faults, in a stress state near to failure, possibly triggered by a slow-slip event, a subvertical fluid transport, or a horizontal dike. Fluids played an important role in the Anydros earthquake source processes, as indicated by two key observations: consistently positive and significant ISO and CLVD components, and evidence for a low friction coefficient. How fluids interact with the existing normal faults—whether by promoting opening, reducing friction, or both—remains unresolved and will require dedicated numerical modeling to clarify. In addition to fluids, another qualitatively indicated factor—one that still requires quantitative modeling—is aseis-

mic slip on one or more faults, as suggested by the observed episodes of rapid migration.

Acknowledgements

The authors would like to thank I. Fountoulakis and C. Evangelidis for valuable discussions and for providing the crustal velocity model. We also thank A. Lomax for sharing his location results. Special thanks go to Z. Roumelioti for her participation in the previous stages of this work and numerous insightful discussions. We also thank all the Greek colleagues who maintained networks, deployed new stations, and processed all sorts of data during this remarkable sequence. The code sti2MT.m for the STC model and related routines written by V. Vavryčuk and P. Kolář were used. Jiří Zahradník was supported by the Czech Science Foundation (grant 23-06345S). Efthimios Sokos and Jiří Zahradník were supported by the "TowaRds AdvaNced multidiSciplinary Fault ObseRvatory systeMs^2" (TRANSFORM^2) project. TRANSFORM^2 is funded by the European Union under project number 101188365 within the HORIZON-INFRA-2024-DEV-01-01 call. Finally, we thank the Handling Editor, Meng (Matt) Wei, the Production Editor Andrea Llenos, the Copy and Layout Editor Théa Ragon and the two anonymous reviewers for their constructive comments that significantly improved this manuscript.

7 Data and code availability

Regional waveform data used in this study were obtained from the Hellenic Unified Seismic Network (HUSN) networks: HL, National Observatory of Athens, Institute of Geodynamics, Athens (1975), HC, Technological Educational Institute of Crete (2006), HP, University of Patras (2000), HA, University of Athens (2008). Data from the HL, HC, HP, and HA networks can be accessed through the National Observatory of Athens (NOA) EIDA node https://eida.gein.noa.gr/ (Evangelidis et al., 2021). For StressInverse code of Vavryčuk (2014), see https://www.ig.cas.cz/en/stress-inverse/. The maps were generated using the Generic Mapping Tools v.6, https://www.generic-mapping-tools.org/download/. Our new ISOLA-BaBoo is an open-source code, available in a GitHub repository at the following link: https://github.com/esokos/isola/tree/master/Isola_Release_2024_with_BaBoo. The folders `ISOLA-BaBoo_FORTRAN_2024`, and `ISOLA-BaBoo_GUI_2024` include the FORTRAN and MATLAB parts of the software, respectively. The `Test_Example_and_codes` folder includes subfolder `test_example` (code, data, readme), which serves as a simple, fast test of the code innovations described in this paper, without the need for the installation of the complete ISOLA-GUI software. The test corresponds to the first example of this paper (event no. 19), detailed in Fig. 4, and allows its replication. To run the test, the user should create a standalone folder `test_example` in his/her computer and copy into it the content of subfolder `test_example` from the repository. Then, in `test_example`, the user has all the necessary codes and data and can follow the short manuals denoted there as `readme_CONTENT` and `readme_HOW-TO-RUN`. Finally, in the same GitHub repository, the `Examples_Ev19_Ev20` folder includes additional examples (which need the complete installation of ISOLA-GUI) and are also archived at Zahradník and Sokos (2025a), https://doi.org/10.5281/zenodo.16745285.

8 Competing interest

The authors declare they have no competing interests.

References

Andinisari, R., Konstantinou, K., and Ranjan, P. Seismicity along the Santorini-Amorgos zone and its relationship with active tectonics and fluid distribution. *Physics of the Earth and Planetary Interiors*, 312:106660, Mar. 2021a. doi: 10.1016/j.pepi.2021.106660.

Andinisari, R., Konstantinou, K., and Ranjan, P. Moment tensor inversion of microearthquakes along the Santorini-Amorgos zone: Tensile faulting and emerging volcanism in an extensional setting. *Journal of Volcanology and Geothermal Research*, 420: 107394, Dec. 2021b. doi: 10.1016/j.jvolgeores.2021.107394.

Autumn, K. R., Hooft, E. E. E., and Toomey, D. R. Exploring Mid-to-Lower Crustal Magma Plumbing of Santorini and Kolumbo Volcanoes Using PmP Tomography. *Geochemistry, Geophysics, Geosystems*, 26(4), Apr. 2025. doi: 10.1029/2025gc012170.

Briole, P., Ganas, A., Serpetsidaki, A., Beauducel, F., Sakkas, V., Tsironi, V., and Elias, P. Volcano-tectonic interaction at Santorini. The crisis of February 2025. Constraints from geodesy. *Geophysical Journal International*, 242(3), July 2025. doi: 10.1093/gji/ggaf262.

Brüstle, A. Seismicity of the eastern Hellenic Subduction Zone, Ruhr University [Ph.D. thesis.], 2012.

Bufféral, S., Briole, P., Dupont, A., Escartin, J., and Heinrich, P. Tsunami modelling for a potential earthquake between Santorini and Amorgos (Greece). Extended Abstract. *Proceedings of the 17th International Congress of the Geological Society of Greece*, 2025.

Büyükakpınar, P., Isken, M. P., Heimann, S., Dahm, T., Kühn, D., Starke, J., López Comino, J. A., Cesca, S., Doubravová, J., Gudnason, E. A., and Agústsdóttir, T. Understanding the Seismic Signature of Transtensional Opening in the Reykjanes Peninsula Rift Zone, SW Iceland. *Journal of Geophysical Research: Solid Earth*, 130(1), Dec. 2024. doi: 10.1029/2024jb029566.

Cappa, F., Guglielmi, Y., Nussbaum, C., De Barros, L., and Birkholzer, J. Fluid migration in low-permeability faults driven by decoupling of fault slip and opening. *Nature Geoscience*, 15 (9):747–751, Aug. 2022. doi: 10.1038/s41561-022-00993-4.

Dahm, T. and Brandsdóttir, B. Moment tensors of microearthquakes from the Eyjafjallajökull volcano in South Iceland. *Geophysical Journal International*, 130(1):183–192, July 1997. doi: 10.1111/j.1365-246x.1997.tb00997.x.

Dahm, T. and Krüger, F. Moment tensor inversion and moment tensor interpretation. *New Manual of Seismological Observatory Practice 2 (NMSOP2)*, 2013. doi: 10.2312/GFZ.NMSOP-2_IS_3.9.

Dettmer, J., Dosso, S. E., and Holland, C. W. Uncertainty estimation in seismo-acoustic reflection travel time inversion. *The Journal of the Acoustical Society of America*, 122(1):161–176, July 2007. doi: 10.1121/1.2736514.

Dimitriadis, I., Papazachos, C., Panagiotopoulos, D., Hatzidimitriou, P., Bohnhoff, M., Rische, M., and Meier, T. P and S velocity structures of the Santorini–Coloumbo volcanic sys-

tem (Aegean Sea, Greece) obtained by non-linear inversion of travel times and its tectonic implications. *Journal of Volcanology and Geothermal Research*, 195(1):13–30, Aug. 2010. doi: 10.1016/j.jvolgeores.2010.05.013.

Dodge, Y. *The Concise Encyclopedia of Statistics*. Springer, 2008.

Dou, Z., Gao, T., Zhao, Z., Li, J., Yang, Q., and Shang, D. The role of water lubrication in critical state fault slip. *Engineering Geology*, 271:105606, June 2020. doi: 10.1016/j.enggeo.2020.105606.

Dublanchet, P. and De Barros, L. Dual Seismic Migration Velocities in Seismic Swarms. *Geophysical Research Letters*, 48(1), Jan. 2021. doi: 10.1029/2020gl090025.

Dziewonski, A. M., Chou, T., and Woodhouse, J. H. Determination of earthquake source parameters from waveform data for studies of global and regional seismicity. *Journal of Geophysical Research: Solid Earth*, 86(B4):2825–2852, Apr. 1981. doi: 10.1029/jb086ib04p02825.

Ekström, G., Nettles, M., and Dziewoński, A. The global CMT project 2004–2010: Centroid-moment tensors for 13,017 earthquakes. *Physics of the Earth and Planetary Interiors*, 200–201:1–9, June 2012. doi: 10.1016/j.pepi.2012.04.002.

Evangelidis, C. P., Triantafyllis, N., Samios, M., Boukouras, K., Kontakos, K., Ktenidou, O.-J., Fountoulakis, I., Kalogeras, I., Melis, N. S., Galanis, O., Papazachos, C. B., Hatzidimitriou, P., Scordilis, E., Sokos, E., Paraskevopoulos, P., Serpetsidaki, A., Kaviris, G., Kapetanidis, V., Papadimitriou, P., Voulgaris, N., Kassaras, I., Chatzopoulos, G., Makris, I., Vallianatos, F., Kostantinidou, K., Papaioannou, C., Theodoulidis, N., Margaris, B., Pilidou, S., Dimitriadis, I., Iosif, P., Manakou, M., Roumelioti, Z., Pitilakis, K., Riga, E., Drakatos, G., Kiratzi, A., and Tselentis, G.-A. Seismic Waveform Data from Greece and Cyprus: Integration, Archival, and Open Access. *Seismological Research Letters*, 92 (3):1672–1684, Mar. 2021. doi: 10.1785/0220200408.

Flóvenz, O. G., Wang, R., Hersir, G. P., Dahm, T., Hainzl, S., Vassileva, M., Drouin, V., Heimann, S., Isken, M. P., Gudnason, E. A., Agústsson, K., Agústsdóttir, T., Horálek, J., Motagh, M., Walter, T. R., Rivalta, E., Jousset, P., Krawczyk, C. M., and Milkereit, C. Cyclical geothermal unrest as a precursor to Iceland's 2021 Fagradalsfjall eruption. *Nature Geoscience*, 15(5):397–404, May 2022. doi: 10.1038/s41561-022-00930-5.

Fountoulakis, I. and Evangelidis, C. P. The 2024–2025 seismic sequence in the Santorini-Amorgos region: Insights into volcanotectonic activity through high-resolution seismic monitoring. *Seismica*, 4(1), May 2025. doi: 10.26443/seismica.v4i1.1663.

Ganas, A. NOAFAULTS KMZ layer Version 5.0, 2023. doi: 10.5281/ZENODO.8075517.

Ganas, A., Briole, P., Tsironi, V., Goutsos, G., Madonis, N., Liadopoulos, E., and Mintourakis, I. Geodetic monitoring of the 2024–2025 Santorini volcanic unrest using GNSS and InSAR data: Preliminary results. Extended Abstract. *Proceedings of the 17th International Congress of the Geological Society of Greece*, 2025.

HA, University of Athens. Hellenic unified seismological network, university of athens, seismological laboratory, 2008. doi: 10.7914/SN/HA.

Hallo, M. and Gallovič, F. Fast and cheap approximation of Green function uncertainty for waveform-based earthquake source inversions. *Geophysical Journal International*, 207(2):1012–1029, Aug. 2016. doi: 10.1093/gji/ggw320.

HC, Technological Educational Institute of Crete. Seismological network of crete, 2006. doi: 10.7914/SN/HC.

Heath, B. A., Hooft, E. E. E., Toomey, D. R., Papazachos, C. B., Nomikou, P., Paulatto, M., Morgan, J. V., and Warner, M. R. Tectonism and Its Relation to Magmatism Around Santorini Volcano From Upper Crustal P Wave Velocity. *Journal of Geophysical Research: Solid Earth*, 124(10):10610–10629, Oct. 2019. doi: 10.1029/2019jb017699.

Heimann, S., Isken, M., Kühn, D., Sudhaus, H., Steinberg, A., Daout, S., Cesca, S., Vasyura-Bathke, H., and Dahm, T. Grond - A probabilistic earthquake source inversion framework, 2018. doi: 10.5880/GFZ.2.1.2018.003.

HL, National Observatory of Athens, Institute of Geodynamics, Athens. Hellenic unified seismological network, 1975. doi: 10.7914/SN/HL.

HP, University of Patras. Hellenic unified seismological network, 2000. doi: 10.7914/SN/HP.

Hrubcová, P., Doubravová, J., and Vavryčuk, V. Non-double-couple earthquakes in 2017 swarm in Reykjanes Peninsula, SW Iceland: Sensitive indicator of volcano-tectonic movements at slow-spreading rift. *Earth and Planetary Science Letters*, 563: 116875, June 2021. doi: 10.1016/j.epsl.2021.116875.

Hufstetler, R. S., Hooft, E. E. E., Toomey, D. R., VanderBeek, B. P., Papazachos, C. B., and Chatzis, N. Seismic Structure of the Mid to Upper Crust at the Santorini-Kolumbo Magma System From Joint Earthquake and Active Source Vp-Vs Tomography. *Geochemistry, Geophysics, Geosystems*, 26(4), Apr. 2025. doi: 10.1029/2024gc012022.

Isken, M., Karstens, J., Nomikou, P., Parks, M., Drouin, V., Rivalta, E., Crutchley, G., Haghshenas Haghighi, M., Hooft, E., Cesca, S., Walter, T., Hainzl, S., Saul, J., Anastasiou, D., Raptakis, K., Shapiro, N., Münchmeyer, J., Higueret, Q., Soubestre, J., Brenguier, F., Hufstetler, R., Autumn, K., Tsakiri, M., Lange, D., Kopp, H., and Urlaub, M. Volcanic crisis reveals coupled magma system at Santorini and Kolumbo. *Nature*, 645(8082):939–945, Sept. 2025. doi: 10.1038/s41586-025-09525-7.

Karakostas, V., Lomax, A., Anagnostou, V., Papadimitriou, E., Acocella, V., Hicks, S., and Henry, P. The 2025 seismicity burst in the Santorini–Amorgos seismovolcanic zone. Extended Abstract. *Proceedings of the 17th International Congress of the Geological Society of Greece*, 2025.

Karstens, J., Nomikou, P., Isken, M., Parks, M., Drouin, V., Hooft, E., Walter, T., Haghshenas Haghighi, M., and Anastasiou, D. The 2025 seismic crisis reveals a coupled magma feeding system at Santorini and Kolumbo. Extended Abstract. In *Proceedings of the 17th International Congress of the Geological Society of Greece*, Greece, 2025. Mytilene.

Kühn, D., Heimann, S., Isken, M. P., Ruigrok, E., and Dost, B. Probabilistic Moment Tensor Inversion for Hydrocarbon-Induced Seismicity in the Groningen Gas Field, The Netherlands, Part 1: Testing. *Bulletin of the Seismological Society of America*, 110(5): 2095–2111, Aug. 2020. doi: 10.1785/0120200099.

Křížová, D., Zahradník, J., and Kiratzi, A. Resolvability of Isotropic Component in Regional Seismic Moment Tensor Inversion. *Bulletin of the Seismological Society of America*, 103(4):2460–2473, July 2013. doi: 10.1785/0120120097.

Křížová, D., Zahradník, J., and Kiratzi, A. Possible Indicator of a Strong Isotropic Earthquake Component: Example of Two Shallow Earthquakes in Greece. *Bulletin of the Seismological Society of America*, 106(6):2784–2795, Oct. 2016. doi: 10.1785/0120160086.

Lomax, A. NLL-SSST-coherence high-precision earthquake location catalog for the 2025 Santorini-Amorgos earthquake swarm, 2025. doi: 10.5281/ZENODO.14956645.

Lomax, A., Anagnostou, V., Karakostas, V., Hicks, S. P., and Papadimitriou, E. The 2025 Santorini unrest unveiled: Rebounding magmatic dike intrusion with triggered seismicity. *Science*, 390 (6775), Nov. 2025. doi: 10.1126/science.adz8538.

Martínez-Garzón, P., Kwiatek, G., Bohnhoff, M., and Dresen, G. Volumetric components in the earthquake source related to fluid

injection and stress state. *Geophysical Research Letters*, 44(2): 800–809, Jan. 2017. doi: 10.1002/2016gl071963.

Novotný, O., Zahradník, J., and Tselentis, G. Northwestern Turkey Earthquakes and the Crustal Structure Inferred from Surface Waves Observed in Western Greece. *Bulletin of the Seismological Society of America*, 91(4):875–879, Aug. 2001. doi: 10.1785/0120000116.

Poppeliers, C. and Preston, L. An efficient method to propagate model uncertainty when inverting seismic data for time domain seismic moment tensors. *Geophysical Journal International*, 231 (2):1221–1232, June 2022. doi: 10.1093/gji/ggac227.

Rodriguez, J. E. and Williams, D. R. Bayesian Bootstrapped Correlation Coefficients. *The Quantitative Methods for Psychology*, 18 (1):39–54, Mar. 2022. doi: 10.20982/tqmp.18.1.p039.

Rubin, D. B. The Bayesian Bootstrap. *The Annals of Statistics*, 9(1), Jan. 1981. doi: 10.1214/aos/1176345338.

Rutter, E., Hackston, A., Yeatman, E., Brodie, K., Mecklenburgh, J., and May, S. Reduction of friction on geological faults by weak-phase smearing. *Journal of Structural Geology*, 51:52–60, June 2013. doi: 10.1016/j.jsg.2013.03.008.

Schmid, F., Petersen, G., Hooft, E., Paulatto, M., Chrapkiewicz, K., Hensch, M., and Dahm, T. Heralds of Future Volcanism: Swarms of Microseismicity Beneath the Submarine Kolumbo Volcano Indicate Opening of Near-Vertical Fractures Exploited by Ascending Melts. *Geochemistry, Geophysics, Geosystems*, 23(7), July 2022. doi: 10.1029/2022gc010420.

Sokos, E. and Zahradník, J. Evaluating Centroid-Moment-Tensor Uncertainty in the New Version of ISOLA Software. *Seismological Research Letters*, 84(4):656–665, July 2013. doi: 10.1785/0220130002.

Tape, W. and Tape, C. A geometric setting for moment tensors. *Geophysical Journal International*, 190(1):476–498, May 2012. doi: 10.1111/j.1365-246x.2012.05491.x.

Tarantola, A. *Inverse Problem Theory and Methods for Model Parameter Estimation*. Society for Industrial and Applied Mathematics, Jan. 2005. doi: 10.1137/1.9780898717921.

Triantafyllis, N., Sokos, E., Ilias, A., and Zahradník, J. Scisola: Automatic Moment Tensor Solution for SeisComP3. *Seismological Research Letters*, 87(1):157–163, Dec. 2015. doi: 10.1785/0220150065.

Triantafyllis, N., Venetis, I. E., Fountoulakis, I., Pikoulis, E.-V., Sokos, E., and Evangelidis, C. P. Gisola: A High-Performance Computing Application for Real-Time Moment Tensor Inversion. *Seismological Research Letters*, 93(2A):957–966, Dec. 2021. doi: 10.1785/0220210153.

Vackář, J., Burjánek, J., Gallovič, F., Zahradník, J., and Clinton, J. Bayesian ISOLA: new tool for automated centroid moment tensor inversion. *Geophysical Journal International*, 210(2): 693–705, Apr. 2017. doi: 10.1093/gji/ggx158.

Vavryčuk, V. Tensile earthquakes: Theory, modeling, and inversion. *Journal of Geophysical Research*, 116(B12), Dec. 2011. doi: 10.1029/2011jb008770.

Vavryčuk, V. Iterative joint inversion for stress and fault orientations from focal mechanisms. *Geophysical Journal International*, 199(1):69–77, July 2014. doi: 10.1093/gji/ggu224.

Vavryčuk, V. *Earthquake Mechanisms and Stress Field*, page 1–21. Springer Berlin Heidelberg, 2015. doi: 10.1007/978-3-642-36197-5_295-1.

Waldhauser, F. hypoDD-A Program to Compute Double-Difference Hypocenter Locations. *US Geological Survey, Open-File Report 2001-113*, 2001. doi: 10.3133/ofr01113.

Waldhauser, F. and Ellsworth, W. A Double-Difference Earthquake Location Algorithm: Method and Application to the Northern Hayward Fault, California. *Bulletin of the Seismological Society of America*, 90(6):1353–1368, Dec. 2000. doi: 10.1785/0120000006.

Zahradnik, J., Sokos, E., Roumelioti, Z., and Turhan, F. Positive isotropic components of the 2025 Santorini-Amorgos earthquakes. Feb. 2025. doi: 10.31223/x5rd9s.

Zahradník, J. and Sokos, E. *ISOLA code for multiple-point source modeling –review. In Moment Tensor Solutions - A Useful Tool for Seismotectonics*. Springer International Publishing, 2018. doi: 10.1007/978-3-319-77359-9.

Zahradník, J. and Sokos, E. ISOLA-BaBoo codes and data of two 2025 Anydros earthquake examples., 2025a. doi: 10.5281/ZENODO.16745285.

Zahradník, J. and Sokos, E. ISOLA2024: Assessing and Understanding Uncertainties of Full Moment Tensors. *Seismological Research Letters*, 96(4):2647–2659, Jan. 2025b. doi: 10.1785/0220240420.

Zahradník, J., Sokos, E., Roumelioti, Z., and Turhan, F. Full moment tensors of the 2025 Santorini-Amorgos earthquakes, 2025a. doi: 10.5281/ZENODO.14995536.

Zahradník, J., Sokos, E., Roumelioti, Z., and Turhan, F. Non-shear faulting of the 2025 Santorini-Amorgos (Anydros) earthquakes. Extended abstract 00320. Extended Abstract. *Proceedings of the 17th International Congress of the Geological Society of Greece*, 2025b. https://ege2025lesvos.gr/abstracts/.